Controlling oxide promoter coverage and microstructure on metals of inverse catalysts: Application to liquid phase tetrahydrofurfuryl alcohol conversion to 1,5-pentanediol

Jiahua Zhou [a,b], Jiayi Fu [a,b], Piaoping Yang [a], Kewei Yu [a], Stavros Caratzoulas [b], Weiqing Zheng [b,*], Dionisios G. Vlachos [a,b,**]

[a] *Department of Chemical and Biomolecular Engineering, University of Delaware, Newark, DE 19716, USA*
[b] *Catalysis Center for Energy Innovation, University of Delaware, Newark, DE 19716, USA*

ARTICLE INFO

ABSTRACT

Metal M_1/metal oxide M_2O_x ($M_1M_2O_x$) inverse catalysts, where the oxide layer rests atop metal, have gained attention for their distinct catalytic performance. They are intensively studied in biomass upgrading, e.g., the hydrogenolysis of tetrahydrofurfuryl alcohol to produce 1,5-pentanediol. Pt and MO_x (M = W, Mo, Re, Nb) exhibit remarkable synergism in activity and selectivity, but the active sites remain poorly understood. Here, we examine the influence of oxide loading on $PtMO_x$ inverse catalysts and introduce a high-pressure wash treatment to leach the excess oxide from carbon and optimize their structure. The findings reveal a saturation sub-monolayer MO_x coverage with 2D atomic structure on Pt that is crucial for performance; excessive loading leads to nanocrystalline of lower activity, and low loading exposes unselective metal sites. Wash treatment selectively removes MO_x from carbon, enhances their dispersion on Pt, and improves, in most cases, the performance. Tuning the inverse structure advances structure-reactivity understanding.

1. Introduction

Metal-metal oxide ($M_1M_2O_x$) catalysts play a pivotal role in a range of applications [1–7] due to their unique catalytic performance. Among these catalysts, those with an inverse configuration, where the oxide layer is positioned atop a metal [8,9], have gained significant attention for their distinctive characteristics. Notable examples [10–18] include nanoparticles of noble metals, such as Pt, Ir, or Rh, coated with reducible and oxophilic metal oxides, like WO_x, MoO_x, ReO_x, and NbO_x, all anchored on diverse support matrices. This configuration opens exciting possibilities for catalytic transformations. These catalysts are multi-functional: the metal splits H_2 that spills over and hydroxylates the oxide, creating Brønsted acid sites.

One prominent chemistry extensively investigated is the hydrogenolysis of tetrahydrofurfuryl alcohol (THFA) on $PtMO_x$/C to produce 1,5-pentanediol [10,11,19,20]. This reaction serves as an excellent model system to study the catalyst performance. What makes these catalysts especially intriguing is that their components demonstrate a strong synergistic interaction when the oxide overlayer is in sub-monolayer coverage [10,11,21–23]. Increasing metal oxide loading can lead to excess deposition onto the support, formation of nanocrystalline structures on the metal with lower Brønsted acidity and covering of the metal sites. It requires precise control to ensure sub-monolayer coverage on Pt. Still, it presents challenges [8,9,24] from uncertainties in loadings and complex interactions of metal oxides and support materials. While atomic layer deposition (ALD) [8,11] offers control over loadings, it is not as widespread. Common methods, such as impregnation [9,24], frequently result in the unintended deposition of metal oxides onto the support. Optimizing the synthesis is imperative.

It has been reported that early transition metal oxides anchored on supports can be mobile under high-pressure hydrogen and solution (such as water) [19,20,25]. Here, we explore this idea to optimize the synthesis of powder inverse catalysts. We synthesize a library of $PtMO_x$/C (M = W, Mo, Re, Nb) inverse powder catalysts and use high-pressure H_2 and water to conduct wash treatment. By combining X-ray photoelectron spectroscopy (XPS) and CO chemisorption, we

---

* Corresponding author.
** Corresponding author at: Department of Chemical and Biomolecular Engineering, University of Delaware, Newark, DE 19716, USA.
E-mail addresses: weiqing@udel.edu (W. Zheng), vlachos@udel.edu (D.G. Vlachos).

demonstrate that some of the metal oxides can be washed off from the carbon surfaces, and the MO_x coverage on Pt can be enhanced. Using the THFA ring opening reaction as a probe, we elucidate that the wash treatment can redisperse the MO_x structure from nanocrystalline into 2D atomic structure with sub-monolayer coverage on Pt surfaces and improve reactivity. Our work illustrates the potential for fine-tuning the inverse Pt-MO_x structure and improving ring opening reactivity.

2. Methods

2.1. Catalyst synthesis

PtMO$_x$/C inverse catalysts were synthesized using a sequential impregnation method. To prepare Pt/C, 2.4 g of carbon black (Vulcan XC-72R) was mixed with 2.4 mL of a precursor solution comprising 0.19 g of tetraammineplatinum(II) nitrate (Pt(NH$_3$)$_4$(NO$_3$)$_2$ 99.99%, 13897, Alfa Aesar), and 25 vol% ethanol in deionized water (Harleco). The mixture was stirred for 1.5 h with a glass rod in a heated 100 mL beaker (the temperature of the hot plate was set to 70 °C), and then stirred for 0.5 min every 20 min for an additional 2 h. The mixture was left on the hot plate for 1.5 h or until no steam condensed on the beaker wall. Subsequently, the powder was dried further in an oven at 110 °C overnight. The resulting powder was reduced at 500 °C in a quartz boat placed at the center of a tubular furnace using a flowing mixture of 10% H$_2$/He at a flow rate of 200 mL/min. The furnace ramp rate was 10 °C/min, and the holding time was 2 h. Before removing the sample at room temperature, the furnace was purged with He at 200 mL/min for 10 min. The final Pt/C catalyst contained 4 wt% Pt.

(x wt%) PtMO$_x$/C samples were prepared by using the Pt/C synthesized above. "x" indicates the weight percent of a metal oxide relative on Pt/C (assuming oxides in fully oxidized states, i.e., WO$_3$, MoO$_3$, Re$_2$O$_7$, and Nb$_2$O$_5$). To synthesize (4 wt% WO$_x$) PtWO$_x$/C, ammonium metatungstate hydrate (463922, Sigma-Aldrich) was dissolved in a 1.4 mL mixture of ethanol and water (1:3 vol ratio). Then, the solution was mixed with 0.5 g of Pt/C in a 50 mL beaker. The resulting slurry was continuously stirred at 70 °C for 1 h, followed by intermittent stirring for 0.5 min every 20 min over 2 h. The catalyst powder was left on a hot-plate for a minimum of 1 h before being dried overnight in an oven at 110 °C. Subsequently, the sample underwent annealing at 500 °C in a flowing helium (He) atmosphere at 100 mL/min for 2 h to eliminate ligands. The furnace was programmed with a ramping rate of 10 °C/min. A similar procedure was employed to synthesize (4 + 4 wt% WO$_x$) PtWO$_x$/C using (4 wt% WO$_x$) PtWO$_x$/C as the precursor instead of Pt/C. Likewise, (x wt% MoO$_x$) PtMoO$_x$/C catalysts were synthesized using the same procedure, employing ammonium molybdate (para) tetrahydrate (A13766, Alfa Aesar) as the precursor. To synthesize (x wt% ReO$_x$) PtReO$_x$/C, we employed ammonium perrhenate(VII) (11410, Alfa Aesar) as the precursor. To ensure the stability of Re$_2$O$_7$ and prevent its evaporation, the Re precursor underwent decomposition within a 100 mL/min flow of a 10% H$_2$-He mixture. For NbO$_x$, common niobium precursors like ammonium, niobate (V), oxalate hydrate, and niobium (V) oxalate hydrate do not effectively cover the Pt surface when synthesized using the method mentioned above. Consequently, the PtNbO$_x$/C inverse catalysts with x wt% NbO$_x$ were synthesized by using tetrakis (2, 2, 6, 6-tetramethyl-3, 5-heptanedionato) niobium (IV) as the precursor. To fully dissolve 1 g of the precursor at room temperature, 234 mL of acetone was required. Due to the larger volume of the precursor mixture compared to the pore volume of Pt/C, we repeated the mixing and drying steps. For each 0.5 g of Pt/C, we introduced 8.3 mL of the precursor solution into the powder and subjected it to continuous stirring at 35 °C for 0.5 h. Upon achieving powder-like consistency, an additional 8.3 mL of precursor solution was added until the desired quantity of Nb precursor had been impregnated onto the Pt/C catalyst. Subsequently, the sample underwent overnight drying in the oven at 110 °C, followed by a decomposition at 400 °C in a flowing helium atmosphere (100 mL/min) for 2 h. Finally, oxidization was carried out in static air at 200 °C within the muffle furnace.

2.2. Catalyst performance evaluation

The tetrahydrofurfuryl alcohol (THFA) (Sigma Aldrich) ring-opening reaction was performed in a 50 mL high-pressure stainless-steel Parr reactor (Parr Instrument Company). A 10 mL reaction solution containing 1 wt% THFA in deionized water (Harleco) was prepared. To compare catalysts with the same oxide promoter but different metal oxide loadings, we adjusted the catalyst amount to ensure an equal Pt content in the reactor. The reactor underwent three purging cycles (20 bar) with N$_2$ and H$_2$ separately before being pressurized to 35 bar and gradually heated to 140 °C over approximately 20 min. We designated the time when the reactor reached 140 °C as the initial time (as reaction time zero). After 4 h of reaction, the reactor was rapidly cooled in an ice and water mixture bath. The post-reaction solution was purified using a syringe filter and then analyzed using an Agilent 7890 A gas chromatography (GC) system, featuring a flame ionization detector and an HP-INNOWAX-19091 N column. The remaining catalyst powder was separated using a vacuum filtration setup for further characterization.

The gas-phase *tert*-Butanol dehydration reaction was conducted in a home-made fixed-bed reactor operating at near-ambient pressure. The reactor featured a resistance furnace, an online GC system (Agilent 7890B) equipped with a flame ionization detector and a HP Plot-Q column, three mass flow controllers from Brooks instruments for the flows of N$_2$, H$_2$, and He, and a saturator for introducing *tert*-Butanol (Sigma-Aldrich). To control the *tert*-Butanol flow rate, we adjusted the saturator's temperature and the flow rates of the carrier gas (N$_2$) and the balance gas (He). All the pipelines were maintained above 150 °C to prevent condensation. In each experiment, the catalyst bed was positioned between two inert quartz beds within a quartz tube. The catalyst bed temperature was monitored by placing a thermocouple at the center of the bed, which was covered by a quartz sleeve. Before commencing the dehydration reaction, the catalyst underwent annealing in a flowing He-N$_2$ mixture (50% He and 50% N$_2$, 100 mL/min) for 1 h, with a temperature ramp rate of 5 °C/min. Throughout the reaction, the concentration of the *tert*-Butanol was maintained at approximately 4 mol%, with a total flow rate of 100 mL/min. The yield of hydrocarbons, the selectivity of isobutene and isobutane, and the dehydration rate were calculated from

$$yield\ of\ total\ hydrocarbons\ (\%) = \frac{n_{isobutene}\ (mol)\ +\ n_{\ isobutane}(mol)}{n_{initial_{t-BuOH}}\ (mol)} \times 100\%$$

(1)

$$isobutene\ or\ isobutane\ selectivity\ (\%) = \frac{n_{isobutene\ or\ isobutane}\ (mol)}{n_{total\ hydrocarbon}\ (mol)} \times 100\%$$

(2)

$$dehydration\ rate = \frac{(yield_{isobutene} + yield_{isobutane}) \times n_{initial_{t-BuOH}}\ (mol)}{reaction\ time\ (s) \times m_{cat}(g)}$$

(3)

2.3. Catalyst washing experiments

The catalyst washing treatment was conducted in a 50 mL high-pressure stainless-steel Parr reactor. 100 mg catalyst was combined with 10 mL of deionized water (Harleco) in the Parr reactor. The reactor was charged with 35 bar H$_2$, stirred at 300 rpm, and heated to 140 °C using a heating band and a PID temperature controller. The treatment time was set to t = 0 when the reactor reached the target temperature. After each experiment, the reactor was quenched in an ice bath, and the catalyst powder was separated using a vacuum filtration setup, washed with IPA for 3 times, and then dried in an oven at 110 °C overnight.

2.4. Catalyst characterization

2.4.1. XRD

Powder X-ray diffraction (XRD) measurement was conducted within the 2θ range of 10° to 90° using a Cu Kα radiation X-ray source (45 kV, 40 mA, λ = 1.5418) and an X'pert powder diffractometer from Philips.

2.4.2. XRF

Elemental analysis was performed on X-ray fluorescence (XRF) using a Rigaku WDXRF.

2.4.3. Pulse CO chemisorption and H_2 temperature-programmed reduction (H_2-TPR)

CO chemisorption measurements were performed using an Auto Chem II 2920 instrument from Micromeritics in pulse mode, with CO as the probe gas and He as the carrier gas. Approximately 50 mg of sample were used for each measurement. Before CO adsorption, the samples underwent reduction under a 10% H_2/Ar atmosphere, raising the temperature to 250 °C at a ramp rate of 10 °C/min for PtMO$_x$/C (M = W, Mo, Nb) and 120 °C for PtReO$_x$/C to reduce the formation of metallic Re for 1 h. Subsequently, the samples were cooled to 38 °C under a flow of He for 60 min. The 10% CO/Ar mixture was introduced into the catalyst until saturation, indicated by the constancy in the peak area. The waiting time between consecutive pulses was 6.8 min, and 10 pulses were used. The fraction of metal covered by MO$_x$ (MO$_x$ coverage) was determined with a stoichiometry factor of Pt/CO equal to 1

$$MO_x \ Coverage_{Pt \ covered \ by \ MO_x} = \frac{(CO_{uptake(Pt/C)} - CO_{uptake(PtMO_x/C)})}{CO_{uptake(Pt/C)}} \times 100\%$$

(4)

H_2 temperature-programmed reduction (H_2-TPR) was carried out using an AutoChem II 2920 instrument from Micromeritics, equipped with a TCD detector. Approximately 50 mg of the freshly prepared catalyst was initially annealed under a flow of helium at 200 °C for 1 h and then cooled to room temperature. For H_2-TPR, we heated the catalysts to 900 °C, at a ramping rate of 10 °C/min in a mixture of 10 vol% H_2/Ar (with a flow rate of 50 mL/min).

2.4.4. TEM and High-angle annular dark-field STEM (HAADF-STEM)

TEM images were taken on a JEM-2010 F (JEOL, Japan) transmission electron microscope operating at an accelerating voltage of 200 kV. The powdered sample was suspended in acetone through sonication and subsequently loaded onto a porous copper grid that was coated with a holey lacey carbon membrane. The solvent evaporated at room temperature. The high-angle annular dark-field STEM (HAADF-STEM) images and EDS elemental mapping were conducted using a JEOL NEOARM microscope equipped with a probe-forming optics spherical aberration corrector and two large-area energy-dispersive X-ray spectrometers, allowing for swift atomic-resolution EDS mapping. The Pt particle sizes were determined using > 200 count and $d_{TEM} = \sum n_i d_i^3 / \sum n_i d_i^2$, where n_i is the number of particles of diameter d_i.

2.4.5. X-ray photoelectron spectroscopy

The surface composition and atomic ratio were characterized by XPS in a Thermo Fisher K-Alpha Instrument equipped with an Al (K) X-ray source. The sample powder was pressed to a clean, thin Cu foil. Pt 4f, W4f, Mo 3d, Re 4f, O 1s, and C 1s spectra were collected. XPS data analysis was performed with the CasaXPS version 2.3.23PR1.0 software. The atomic ratio of Pt/M was calculated from the core-level spectra of the elements, with the relative sensitivity factors Pt 4f 16.68, W 4f 11.06, Mo 3d 11.01, Re 4f 10.46, C 1s 1, O 1s 2.88 using

$$\frac{n_i}{n_j} = \frac{I_i/S_i}{I_j/S_j}$$

(5)

2.5. Wulff construction and terrace site density estimation

A 1.6 nm Pt nanoparticle with minimized total surface energy was built using the Wulff construction approach included in the Atomic Simulation Environment (ASE) [26] and literature surface energies of (111), (100), and (110) [27].

3. Results and discussion

3.1. Synthesis and characterization of the PtMO$_x$/C (M = W, Mo, Re, Nb) inverse catalysts

We synthesized a library of Pt-metal oxide (PtMO$_x$) inverse catalysts supported on carbon by sequential impregnation [8,9,11] by depositing first 4 wt% Pt (Pt/C) and decorating it with oxophilic metal oxides thereafter with varying the MO$_x$ to Pt molar ratio (Table S1). This method is efficient in synthesizing inverse catalysts for various noble metals (Ru, Rh, Pd, Ir, and Pt) and oxophilic metal oxides (MoO$_x$, VO$_x$, ReO$_x$, WO$_x$, etc.) supported on carbon and SiO$_2$ [9,24]. The oxides (MO$_x$ = WO$_x$, MoO$_x$, ReO$_x$, and NbO$_x$) were selected due to their properties [8–10,21] and applications in biomass upgrading [10,15–18,28,29].

We have previously shown that CO chemisorption is effective for determining the Pt surface covered by the oxide, as Pt strongly adsorbs CO, whereas the metal oxide does not, and the metal surface area decreases upon depositing the metal oxide [8,9,24,30–33]. The CO chemisorption results, summarized in Fig. 1a, Fig. S1, and Table S1, suggest varying degrees of covered Pt surfaces, ranging from 0% (Pt/C) to ~50% (high metal oxide loadings), by increasing the metal oxide loading (MO$_x$/Pt molar ratio). The coverage of the oxide of PtWO$_x$, PtMoO$_x$, and PtNbO$_x$ saturates at ~50% when the metal oxide loading exceeds 5 wt% (a MO$_x$/Pt molar ratio > 1, Fig. 1a and Table S1), whereas PtReO$_x$ requires higher loadings, typically around 15 wt% (a ReO$_x$/Pt ratio of ~3.5). Fig. S2, Fig. 1b, and Fig. S3a-b show representative TEM and HAADF-STEM images of the Pt/C (before MO$_x$ deposition) and PtMoO$_x$/C with highly dispersed Pt nanoparticles and an average size of ~1.6 nm. Figs. S3c-f present bright-field TEM images of PtReO$_x$/C (Fig. S3c-d) and PtNbO$_x$/C (Fig. S3e-f) that show similar configurations to PtWO$_x$/C [8,24] and PtMoO$_x$/C. Recent calculations revealed that the WO$_x$ species adsorb on the terrace rather than on the edge sites of Pt [10,34]. To estimate the proportion of terrace sites on Pt nanoparticles with an average size of ~ 1.6 nm, we calculated the equilibrium morphologies using the Wulff construction. Fig. 1b shows that a 1.6 nm Pt nanoparticle has about 50% surface terrace sites and provides rationalization for why MO$_x$ coverages on Pt saturate at 50%, irrespective of increasing the MO$_x$ loading. To further increase the MO$_x$ coverage on Pt, a repetitively impregnating step was adopted. As shown in Fig. 1a and Table S1, depositing an additional 4% WO$_x$ onto the 4 wt% PtWO$_x$/C enhanced the coverage to 60% (slightly higher than a single deposition of 8% WO$_x$ on Pt/C).

The inverse configuration of PtMO$_x$/C catalysts was further confirmed by high-angle annular dark-field scanning transmission electron microscopy (HAADF-STEM) and energy-dispersive spectroscopy (EDS) mapping. High-resolution EDS elemental mapping analysis, shown in Fig. 1c, reveals that the majority of MoO$_x$ is located on top of Pt nanoparticles with sub-monolayer coverage as Pt and Mo signals align. There is a fraction of MoO$_x$ clusters anchored on the carbon support.

3.2. Tetrahydrofurfuryl alcohol (THFA) ring-opening performance over PtMO$_x$/C inverse catalysts

The synthesized inverse catalysts were evaluated in THFA ring-opening (RO) chemistry [10,11] producing 1,5-pentanediol (1,5-PeD) as the target product. Scheme 1 outlines the key pathways. Pathway I represents the desired ring-opening reaction of β C-O bond scission and hydrogenation to 1,5-PeD. 1,5-PeD can undergo further reaction to 1-pentanol (1-PeOH) by dehydration-hydrogenation, tetrahydropyran
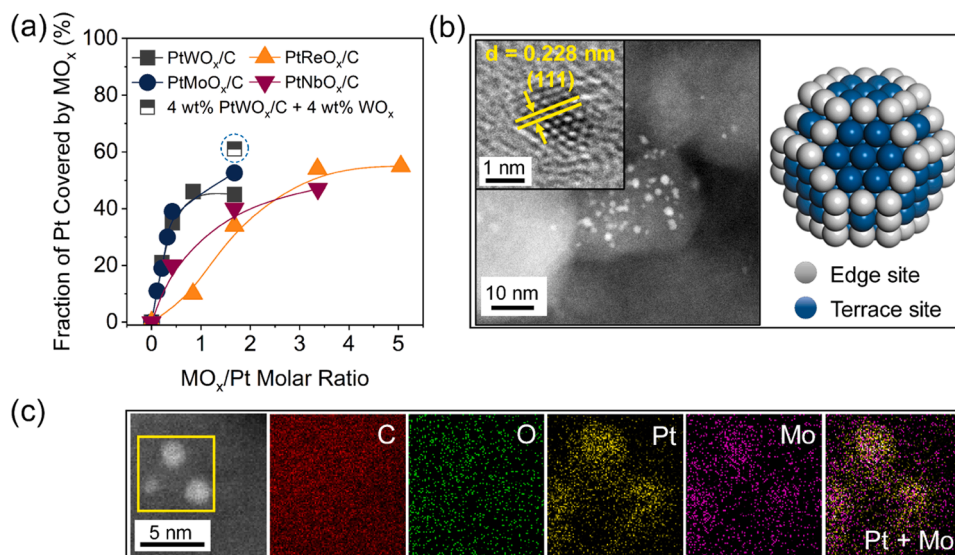
Fig. 1. Structural characterization of PtMO$_x$/C inverse catalysts. (a) Fraction of Pt covered by MO$_x$ vs. MO$_x$ (M = W, Mo, Re, Nb) loading determined by CO chemisorption. (b) HAADF-STEM image of PtMoO$_x$/C fresh catalyst, and high magnification image indicating a lattice spacing of 2.28 Å, and equilibrium morphologies of Pt nanoparticle based on the Wulff construction. (c) HAADF-STEM images and corresponding EDS elemental mapping of the fresh (1.24 wt%) PtMoO$_x$/C inverse catalyst.
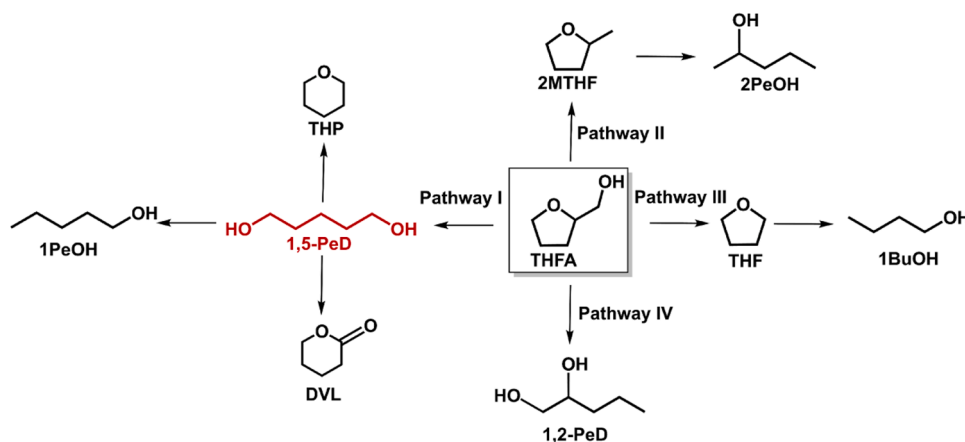
Scheme 1. Reaction network of the THFA reaction over inverse catalysts. Acronyms: **THP** (tetrahydropyran), **DVL** (δ-valerolactone), **1PeOH** (1-pentanol), **1,5-PeD** (1,5-pentanediol), **THFA** (tetrahydrofurfuryl alcohol), **2MTHF** (methyl tetrahydrofuran), **2PeOH** (2-pentanol), **THF** (tetrahydrofuran), **1BuOH** (1-butanol), **1,2-PeD** (1,2-pentanediol). **Pathway I**: ring-opening to 1,5-PeD as an intermediate; **Pathway II** hydrodeoxygenation (dehydroxylation/hydrogenation); **Pathway III** hydroxymethyl group removal; **Pathway IV** direct ring-opening.

(THP) via intramolecular etherification, and δ-valerolactone (DVL) through THFA isomerization to 2-hydroxy tetrahydropyran followed by dehydrogenation. Hydrodeoxygenation of the primary C-O bond leads to 2-methyl tetrahydrofuran (Pathway II) and directs RO to 1,2-pentanediol (1,2-PeD) (Pathway IV). Alternatively, the reaction can follow C-COH bond hydrogenolysis, producing tetrahydrofuran (Pathway III). Previous investigations of THFA reaction over RhReO$_x$ [19,20,35], PtWO$_x$ [10,11], RhMoO$_x$ [25], and others [13] exposed high catalytic activity and selectivity, particularly toward terminal diols. The hydroxyl groups on metal oxide surfaces are dynamic and pivotal in the mechanism [8,9,24]. They can form alkoxide surface intermediates with the side hydroxyl of THFA [36] or serve as Brønsted acid sites [19,34] to protonate the ring oxygen of THFA, yielding an oxocarbenium intermediate.

Fig. 2 illustrates the product distribution (yield, conversion, and selectivity) as a function of metal oxide loading. Notably, the 4 wt% Pt/C catalyst exhibits low activity (~9% of yield and 0.7% of 1,5-PeD selectivity) and higher selectivity toward cleaving more accessible C-C and C-O bonds to side products (Pathways II, III, and IV in Scheme 1).

The MO$_x$/C (M = W, Mo, Re, and Nb) catalysts are almost inactive. Only metal oxide shells on Pt drive the desired Pathway I, demonstrating a strong synergistic effect previously reported [11], with the metal sites dissociating H$_2$ that spills over the oxide to form Brønsted acid sites for selectively breaking the β C–O bond.

For PtWO$_x$ (Fig. 2a) and PtMoO$_x$ pairs (Fig. 2b), the product yield (~40%) and 1,5-PeD selectivity (> 80%) peak at MO$_x$ sub-monolayer loadings (2–4 wt% for WO$_x$ and 1.2 wt% for MoO$_x$, and a coverage on Pt of ~50%) and subsequently decline with increased MO$_x$ loadings. For the PtReO$_x$, the 1,5-PeD yield grows with increasing ReO$_x$ loading and requires much higher loading (~25 wt%, Table S1, and Fig. 1a) to be comparable with PtWO$_x$ and PtMoO$_x$. The PtNbO$_x$ catalysts have low THFA conversion and poor 1,5-PeD selectivity. To assess the influence of incorporated MO$_x$ species on Pt oxidation states (or electronic states) and its consequential impact on the reaction reactivity, we investigated the Pt oxidation states in PtMO$_x$ inverse catalysts using XPS. Fig. S4 and Table S2 imply that the fraction of Pt(0) and Pt(II) fractions in the PtMO$_x$ inverse catalysts are comparable, These observations indicate that Pt
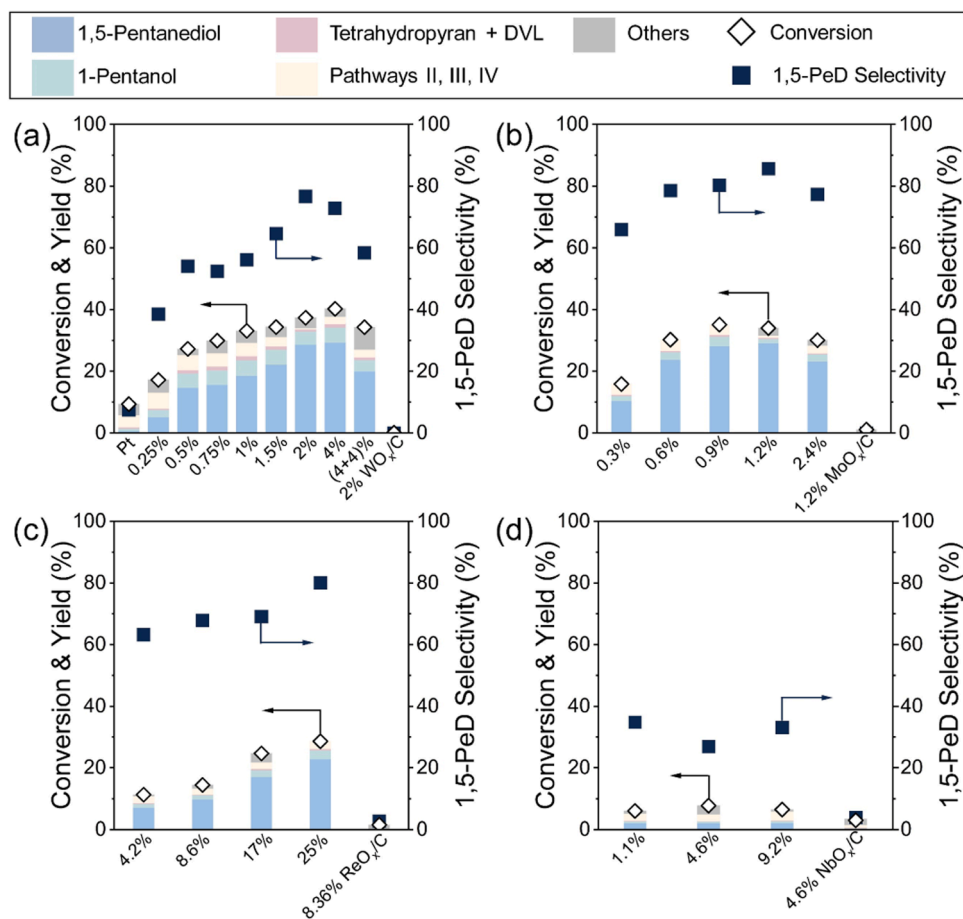
Fig. 2. Performance of the PtMO$_x$/C inverse catalysts. (a)-(d) product distributions over (a) PtWO$_x$/C, (b) PtMoO$_x$/C, (c) PtReO$_x$/C, and (d) PtNbO$_x$/C. Reaction conditions: 4 h, 140 °C, 35 bar H$_2$ measured at room temperature, 10 mL THFA/H$_2$O mixture (concentration: 1 wt% THFA). Catalyst amounts: $100 \times (1 + \alpha\%)$ mg, $50 \times (1 + \alpha\%)$ mg, $25 \times (1 + \alpha\%)$ mg, and $100 \times (1 + \alpha\%)$ mg, respectively, adjusted to achieve < 50% conversion. α% is the metal oxide loading. Selectivity refers to 1,5-PeD (Scheme 1).

oxidation states may not be pivotal factors influencing the conversion and selectivity of the reaction. Clearly, the reactivity of PtMO$_x$ inverse pairs is complex in terms of the role of the metal oxide.

To compare the intrinsic reactivity with varying metal oxide loading, we calculate the THFA rate by normalizing it by the total MO$_x$ loading in moles. Fig. 3 depicts the RO rate and metal oxide coverage against the total MO$_x$ loading. The reactivity order for a similar MO$_x$ coverage (approximately 40%) is PtMoO$_x$/C (1.24 wt% MoO$_x$) > PtWO$_x$/C (2 wt% WO$_x$) > PtReO$_x$/C (8.36 wt% ReO$_x$) >> PtNbO$_x$/C (4.6 wt% NbO$_x$). This order may be attributed to variations in the secondary C–O bond cleavage barriers caused by different interfacial PtMO$_x$ sites, varying effectiveness of Brønsted acid sites on the metal oxides [34], discussed next, or different amounts of the oxide on the carbon. To eliminate the influence of the MO$_x$ on carbon support, we also normalized the rate using the MO$_x$ on Pt instead of the total. The RO rate remains nearly constant with varying MO$_x$ coverage, yet it varies among oxides (Table S3). This analysis indicates that the reduction in the RO rate shown in Fig. 3 is primarily due to the dispersion of the less active sites of oxides on carbon. It also underscores that the active sites possess similar strength with increasing coverage.

To investigate the Brønsted acidity of the inverse catalysts, we employed the kinetics of *tert*-Butanol dehydration as a probe [8,9,24]. As shown in Fig. S5, PtNbO$_x$ exhibits an order of magnitude lower dehydration rate (~0.13 s^{-1}) compared to other PtMO$_x$ pairs (> 1 s^{-1}), suggesting a lower density of Brønsted acid sites and/or weaker Brønsted acid sites on the former. Due to its low reactivity, we do not further discuss this catalyst. The initial dehydration rate of the fresh PtReO$_x$/C is

about 6 s^{-1}, which dropped significantly with co-feeding H$_2$ (Fig. S5c). The inherent facile reduction of ReO$_x$, further enhanced by Pt, leads to its rapid dehydroxylation [12,37] upon H$_2$ exposure. As shown in Fig. S6c, the H$_2$-TPR depicts that ReO$_x$ reduces below 300 °C and as low as 100 °C on PtReO$_x$. While the THFA RO reactivity of the PtReO$_x$/C (Fig. 2c) increases steadily with rising ReO$_x$ loading, its estimated RO rate remains significantly lower than WO$_x$ and MoO$_x$ (Fig. 3c). This disparity could stem from the diminished Brønsted acidity due to the ReO$_x$'s lower oxidation state under high H$_2$ pressure, as noticed by Falcone et al. and Chia et al. [12,37] or the formation of crystallites (Re$_2$O$_7$ or ReO$_3$) of a lower Brønsted acidity. Notably, XRD diffraction patterns of ReO$_3$ appear at higher ReO$_x$ loadings (Fig. S7c) and the spent PtReO$_x$/C catalyst (Fig. S8), indicating ReO$_3$ segregation and sintering with higher loading or upon H$_2$ exposure. These observations indicate that the THFA RO to 1,5-PeD requires a unique atomic environment of clusters of MO$_x$ on top of metal surfaces in the sub-monolayer coverage, in line with our previous investigations on inverse catalysts for simple dehydration of alcohols [8–10,24]. Enhancing the MO$_x$ loading leads to a substantial portion of MO$_x$ being deposited on carbon or forming nanocrystallites on metal surfaces, reducing the metal-metal oxide interfacial sites or the acidity of the Brønsted acid sites provided by the metal oxide on top of Pt.

It was reported that WO$_x$ species are highly mobile under a reducing environment or high-pressure liquid phase reaction conditions [11,19, 25]. Given this, the stability of WO$_x$ on Pt and carbon was assessed through characterization of the 2 wt% PtWO$_x$/C spent catalyst, using XPS and CO chemisorption, as shown in Fig. 4. Notably, the performance
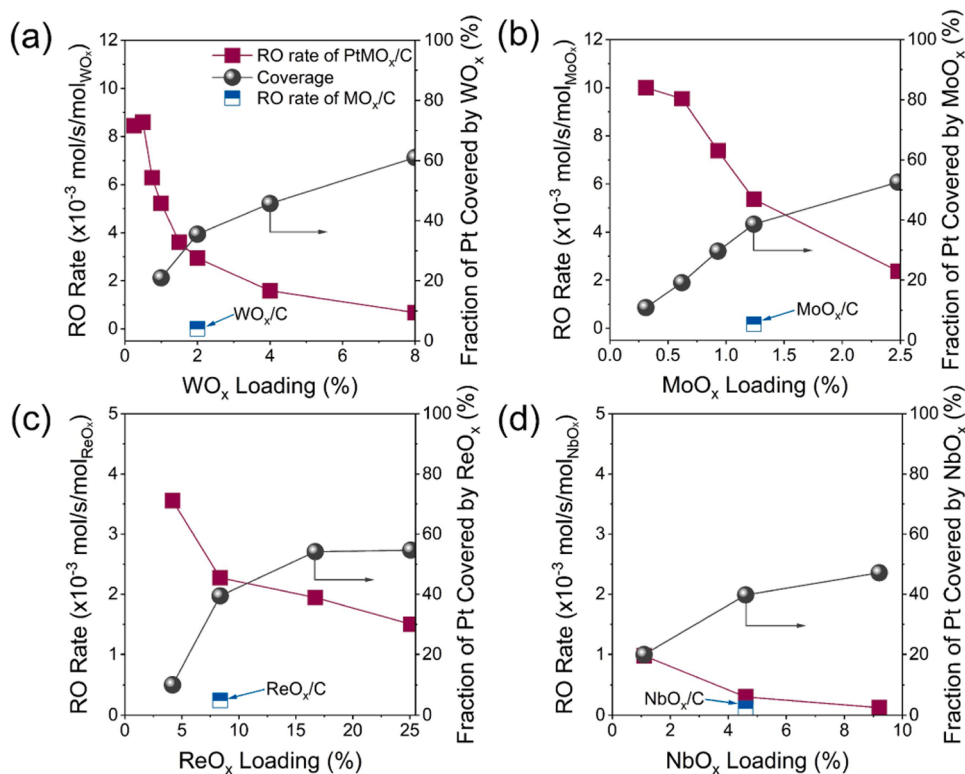
Fig. 3. Total rates of the PtMO$_x$/C inverse catalysts and fraction of Pt covered by metal oxide vs. total metal oxide loading. (a)-(d) ring-opening rates over (a) PtWO$_x$/C, (b) PtMoO$_x$/C, (c) PtReO$_x$/C, and (d) PtNbO$_x$/C. Rates are normalized by the amount of MO$_x$. Reaction conditions: 4 h, 140 °C, 35 bar H$_2$ measured at room temperature, 10 mL THFA/H$_2$O mixture (concentration: 1 wt% THFA). Catalyst amounts: $100 \times (1+\alpha\%)$ mg, $50 \times (1+\alpha\%)$ mg, $25 \times (1+\alpha\%)$ mg, and $100 \times (1+\alpha\%)$ mg, respectively, adjusted to achieve < 50% conversion.
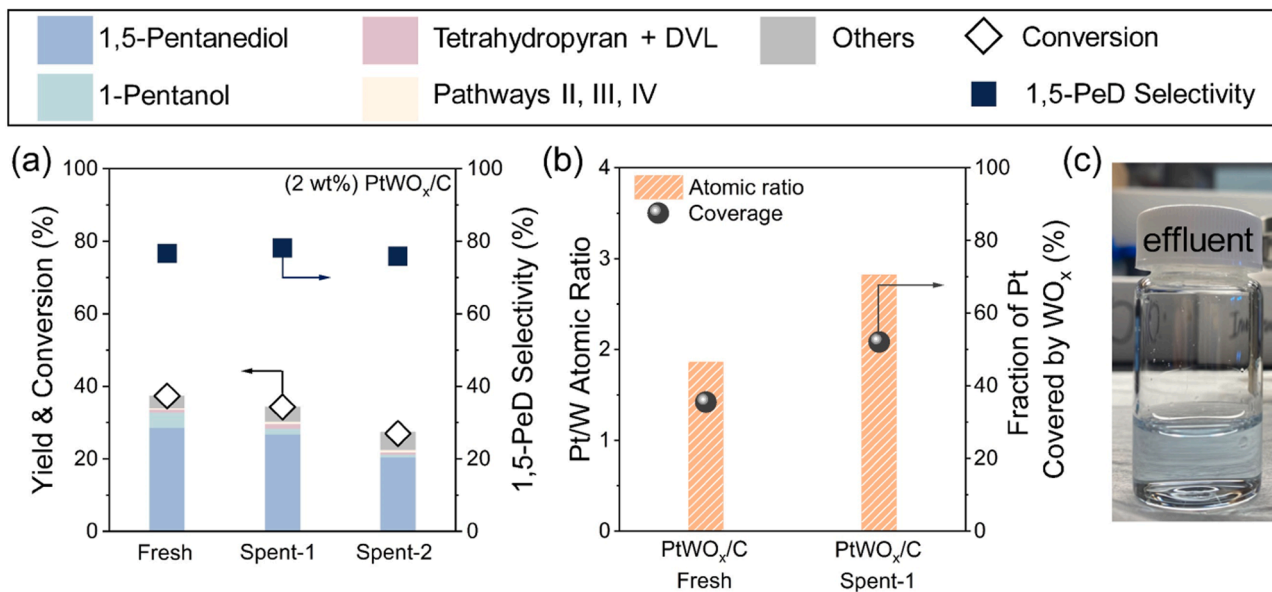

Fig. 4. Spent catalyst activity and stability. (a) Ring-opening reaction performance of the fresh and spent PtWO$_x$/C (2 wt% WO$_x$). Reaction conditions: 4 h, 140 °C, 35 bar H$_2$ measured at room temperature, 10 mL THFA/H$_2$O mixture (concentration: 1 wt% THFA). $100 \times (1+\alpha\%)$ mg, $\alpha = 2$ wt% PtWO$_x$/C. Selectivity refers to 1,5-PeD (Scheme 1). (b) Pt/W atomic ratio and coverage of WO$_x$ on Pt of the fresh and spent catalysts. (c) Picture of the effluent after reaction using fresh PtWO$_x$/C catalyst.

of the spent catalyst is slightly lower than the fresh one (Fig. 4a). As seen in the XPS analysis (Fig. 4b), an estimated 50% of the WO$_x$ was leached into the reaction solution during reaction. This phenomenon was further evidenced by the bluish supernatant of the post-reaction solution (Fig. 4c). Unexpectedly, despite leaching, the coverage of WO$_x$ on Pt in

the spent catalyst increased by approximately 30% (refer to Fig. 4b), further elucidating that the active WO$_x$ species are primarily anchored on Pt at sub-monolayer coverages. This likely stems from the redeposition of WO$_x$ clusters from carbon onto Pt or the redispersion of nanocrystallines of WO$_x$ on Pt into 2D structures. These findings are

consistent with the preference of WO_x species for metal surfaces rather than carbon supports [8,11,24]. To assess the stability of the other pairs, we conducted XPS of the spent $PtMoO_x/C$ and $PtReO_x/C$ (Fig. S9-10). The observed increase in the Pt/M atomic ratio of the spent catalysts, shown in Table S4-6, indicates that MoO_x and ReO_x leach during reaction into the aqueous phase [19] and migrate on the metal. Since the MO_x (M = W, Mo, Re) on carbon is irrelevant to the THFA RO reaction (Fig. 2 and Fig. 3), one could eliminate this phase to provide a better-defined structure with nearly pure inverse configuration. Inspired by these findings, we leach the MO_x from the carbon surfaces after synthesis through high H_2 pressure and wash treatment (see Methods).

3.3. Wash treatment of the Pt-MO_x inverse catalysts

To selectively remove the oxophilic MO_x from carbon surfaces and enhance the density of MO_x 2D atomic structures on Pt, we performed a washing treatment in a high-pressure batch reactor under RO reaction conditions (with water as the solvent). We select (1.24 wt%) $PtMoO_x/C$

as a representative example for HAADF-STEM (Fig. S12). The fresh and washed $PtMoO_x/C$ inverse catalysts exhibit similar mean particle sizes, approximately 1.6 nm, and nearly identical Pt/C (Pt to C) atomic ratios (Fig. S10 and Table S5) according to XPS elemental analysis. This indicates that the metal core remains unchanged in the high-pressure wash treatment.

The CO chemisorption results (Fig. 5a) indicate a 1.25x increase in MoO_x coverage for (1.24 wt%) $PtMoO_x/C$ rising from 38.6% to 48% compared to the fresh samples. The Pt/MoO_x ratio also shows an approximately 21% increase, as observed from both the XPS atomic ratio (Fig. 5a) and the XRF molar ratio (Fig. S13a). To further confirm the inverse structure of the washed samples, we performed the STEM-EDS mapping of the washed $PtMoO_x/C$ catalyst (Fig. 5b), which shows Pt and Mo signals overlapping, as in the fresh catalyst (Fig. 1c). This provides evidence that the wash treatment effectively maintains or possibly enhances the inverse configuration. Fig. 5d compares the THFA RO performance of the fresh and washed $PtMoO_x/C$ inverse catalysts. Notably, the washed $PtMoO_x/C$ exhibited a 39% product yield with 92%
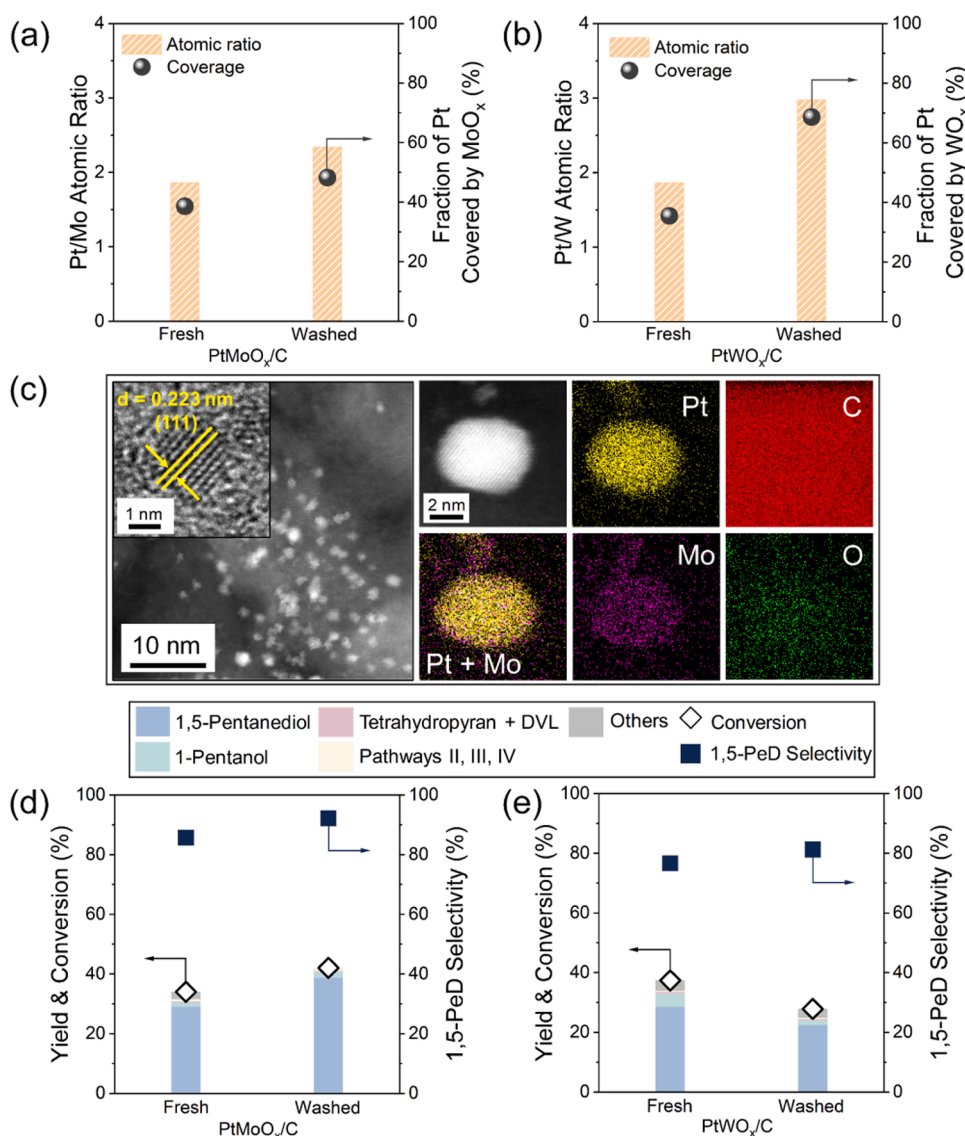

Fig. 5. Redispersion of the oxides through H_2O washing treatment. Pt/M atomic ratio and MO_x coverage on the fresh and washed (a) (1.24 wt%) $PtMoO_x/C$ and (b) (2 wt%) $PtWO_x/C$ inverse catalysts. (c) HAADF-STEM images and EDS elemental mapping of the washed (1.24 wt%) $PtMoO_x/C$ catalyst. Activity of the fresh and washed $PtMO_x/C$ inverse catalysts: (d) (1.24 wt%) $PtMoO_x/C$, (e) (2 wt%) $PtWO_x/C$. Reaction conditions: 4 h, 140 °C, 35 bar H_2 measured at room temperature, 10 mL THFA/H_2O mixture (1 wt% THFA), 50 mg (1.24 wt%) $PtMoO_x/C$, 102 mg (2 wt%) $PtWO_x/C$. Washing was performed using a high-pressure liquid-phase batch reactor. Treatment conditions: 4 h, 140 °C, 35 bar H_2, measured at room temperature, 10 mL water, 100 mg inverse catalyst.

selectivity for 1,5-PeD, outperforming the fresh catalyst of 28% yield and 86% selectivity, further indicating that the wash treatment removes MoO$_x$ from carbon and enhances its dispersion on Pt. To assess the catalyst stability of the washed samples, we employed the washed PtMoO$_x$/C as a representative catalyst in two consecutive runs. As depicted in Fig. S14, its performance of the wash-spent remains comparable to the freshly prepared catalyst. It seems that wash treatment stabilizes the catalyst structure and loading under our conditions.

Turning to the other two oxides, interestingly, the wash treatment had no impact on the PtReO$_x$/C inverse catalysts. Fig. S15 indicates that the Pt/Re atomic ratio, ReO$_x$ coverage, and reactivity of fresh and washed PtReO$_x$/C catalysts remained unchanged, likely due to the facile reduction of ReO$_x$ promoted by Pt. On the contrary, CO chemisorption results shown in Fig. 5b reveal that the WO$_x$ coverage on the washed (2 wt%) PtWO$_x$/C sample increases 2x, rising from 35.5% on the fresh sample to 68.8%. Nevertheless, the activity (Fig. 5e) of the washed PtWO$_x$/C decreased compared to the fresh one. This may be expected, as redeposition enhanced the WO$_x$ coverage above its optimum (Fig. 2a). Overall, washing increases the oxide coverage on the metal surface; its impact on reactivity depends on the initial loading, as indicated in Fig. 2.

Our previous DFT calculations [10] provided insight into the THFA RO pathways on Pt(111) and WO$_x$/Pt(111). On the WO$_x$-modified Pt surface, ring-opening occurs via an oxocarbenium ion-like transition state stabilized by hydrogen bonds with the WO$_x$ hydroxyl groups. The hydrogenation of ring-opened THFA to 1,5-pentanediol uses hydrogen from WO$_x$, created by hydrogen spillover from neighboring Pt atoms to keep replenishing these sites. Our previous studies have also shown that H$_2$ dissociation on Pt is not energetically the rate-limiting step; it occurs rapidly [8,24]. This mechanism highlights the crucial roles of Pt and Pt-WO$_x$ sites in the THFA RO reaction. Scheme 2 shows potential sites on metal/metal oxide catalysts, taking WO$_x$ as an example.

4. Conclusions

In this study, we explored the synthesis and performance of PtMO$_x$ (M=W, Mo, Re, Nb) inverse catalysts supported on carbon for tetrahydrofurfuryl alcohol (THFA) ring-opening to 1,5-pentanediol, a monomer to produce biomass-derived polyesters and polyurethanes. We also introduced a wash treatment method to selectively remove MO$_x$ from carbon surfaces and enhance the density of MO$_x$ 2D atomic structures on Pt, leading typically to improved THFA ring-opening performance. The strong adsorption of MO$_x$ species on the terrace sites of Pt, as opposed to edges, results in a saturation MO$_x$ 2D coverage of approximately 50% on a 1.6 nm Pt nanoparticle (corresponding to about 50% terrace sites based on the Wulff construction). In Scheme 2, we propose that the optimal inverse configuration includes a maximum 2D MO$_x$ submonolayer coverage on the Pt terrace sites, offering an ideal balance of metal and Brønsted acid sites. The metal sites dissociate H$_2$ that diffuses to MO$_x$ surfaces and hydroxylates them. The Brønsted acid sites facilitate ring opening followed by hydrogenation and get regenerated by repeating the cycle. Lower MO$_x$ coverages expose more metal sites, resulting in higher selectivity for primary C-O bond cleavage. Excessive MO$_x$ coverage on Pt reduces the number of metal sites, while a higher MO$_x$ loading leads to nanocrystalline structures with potentially reduced Brønsted acidity [8,9,24] or saturated coverage of Pt terrace sites with less exposed interfacial sites, leading to a decrease in RO activity and selectivity. This explains why the reactivity of the washed PtWO$_x$/C (with 68.8% WO$_x$ coverage) is lower than that of the fresh catalyst (with 35.5% WO$_x$ coverage), while the washed PtMoO$_x$/C (with 48% MoO$_x$ coverage) exhibits higher reactivity compared to the fresh catalyst (with 38.6% MoO$_x$ coverage). The structure and performance depend on the oxide: PtMoO$_x$ and PtWO$_x$ are effective catalysts; PtNbO$_x$ shows poor reactivity and PtReO$_x$ is less efficient due to the facile reducibility of ReO$_x$ catalyzed by Pt.

Overall, this study provides valuable insights into the synthesis/pretreatment and performance of PtMO$_x$ inverse catalysts, shedding
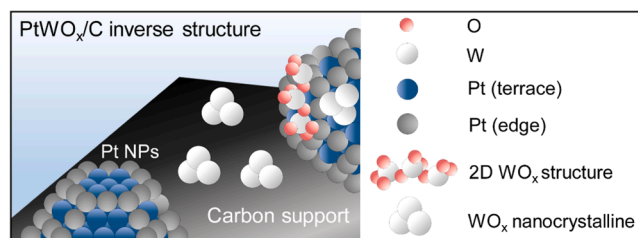
Scheme 2. Potential WO$_x$ structures in PtWO$_x$/C inverse catalysts. The carbon support anchors Pt nanoparticles comprising terrace and edge sites with 2D and nanocrystalline WO$_x$ structures on them and nanocrystalline WO$_x$ structures.

light on the impact of metal oxide structure on catalyst activity and selectivity in the THFA ring-opening reaction.

CRediT authorship contribution statement

Caratzoulas Stavros: Formal analysis, Investigation, Methodology, Supervision, Funding acquisition, Project administration. **Zheng Weiqing:** Formal analysis, Investigation, Methodology, Supervision, Writing – review & editing, Funding acquisition, Project administration. **Yang Piaoping:** Formal analysis, Investigation, Methodology. **Yu Kewei:** Formal analysis, Investigation, Methodology. **Vlachos Dionisios G:** Conceptualization, Formal analysis, Funding acquisition, Project administration, Supervision, Writing – review & editing. **Zhou Jiahua:** Conceptualization, Formal analysis, Investigation, Methodology, Writing – original draft, Writing – review & editing. **Fu Jiayi:** Conceptualization, Formal analysis, Investigation, Methodology.

Author contribution

J.Z. performed the catalyst synthesis, catalyst characterization, experimental kinetics, THFA ring-opening reactivity, catalyst wash treatment, data analysis and prepared the original draft. J.F. initiated the project (synthesized catalysts, conducted THFA ring-opening reactivity tests, and CO chemisorption measurements). P.Y. conducted the Wulff construction and calculated the fraction of terrace sites on Pt nanoparticles. K.Y. and W.Z. performed the HAADF-STEM, EDS mapping, and TEM measurements. D.G.V., W.Z., and S.C. directed the project and guided the experimental and theoretical work. J.Z., W.Z., and D.G.V. wrote the manuscript with input from all authors. J.Z., W.Z., and D.G.V. reviewed, revised, and approved the final manuscript.

Declaration of Competing Interest

The authors declare that they have no known competing financial interests or personal relationships that could have appeared to influence the work reported in this paper.

Data availability

Data will be made available on request.

Acknowledgments

Nanotechnology, supported by the NSF National Nanotechnology Co-ordinated Infrastructure Program under grant number NNCI-2025608.

Appendix A. Supporting information

Supplementary data associated with this article can be found in the online version at doi:10.1016/j.apcatb.2024.123724.

References

[1] I. Ro, J. Qi, S. Lee, M. Xu, X. Yan, Z. Xie, G. Zakem, A. Morales, J.G. Chen, D.G. Vlachos, S. Caratzoulas, P. Christopher, Bifunctional hydroformylation on heterogeneous Rh-WOₓ pair site catalysts, Nature 609 (2022) 287–292, https://doi.org/10.1038/s41586-022-05075-4.

[2] N. Lei, X. Zhao, B. Hou, M. Yang, M. Zhou, F. Liu, A. Wang, T. Zhang, Effective Hydrogenolysis of glycerol to 1,3-propanediol over metal-acid concerted Pt/WOₓ/Al₂O₃ catalysts, ChemCatChem 11 (2019) 3903–3912, https://doi.org/10.1002/cctc.201900689.

[3] L.Z. Qin, M.J. Song, C.L. Chen, Aqueous-phase deoxygenation of glycerol to 1,3-propanediol over Pt/WO₃/ZrO₂ catalysts in a fixed-bed reactor, Green. Chem. 12 (2010) 1466, https://doi.org/10.1039/C0GC00005A.

[4] C. Wang, A.V. Mironenko, A. Raizada, T. Chen, X. Mao, A. Padmanabhan, D.G. Vlachos, R.J. Gorte, J.M. Vohs, Mechanistic study of the direct hydrodeoxygenation of m-Cresol over WOₓ-decorated Pt/C catalysts, ACS Catal. 8 (2018) 7749–7759, https://doi.org/10.1021/acscatal.8b01746.

[5] X. Zhao, J. Wang, M. Yang, N. Lei, L. Li, B. Hou, S. Miao, X. Pan, A. Wang, T. Zhang, Selective hydrogenolysis of glycerol to 1,3-propanediol: manipulating the frustrated lewis pairs by introducing gold to Pt/WOₓ, ChemSusChem 10 (2017) 819–824, https://doi.org/10.1002/cssc.201601503.

[6] B. Zhang, W. Zhou, J. Zhang, Z. Gao, D. Cheng, L. Tang, X. Liu, Y. Song, C. Dong, Y. Xu, J. Yan, M. Peng, H. Liu, M. Douthwaite, M. Wang, D. Ma, Adjacent Pt nanoparticles and sub-nanometer WOₓ clusters determine catalytic isomerization of C₇H₁₆, CCS Chem. 4 (2021) 3371–3382, https://doi.org/10.31635/ccschem.021.202101454.

[7] S. Echeandia, P.L. Arias, V.L. Barrio, B. Pawelec, J.L.G. Fierro, Synergy effect in the HDO of phenol over Ni–W catalysts supported on active carbon: effect of tungsten precursors, Appl. Catal. B: Environ. 101 (2010) 1–12, https://doi.org/10.1016/j.apcatb.2010.08.018.

[8] J. Fu, S. Liu, W. Zheng, R. Huang, C. Wang, A. Lawal, K. Alexopoulos, S. Liu, Y. Wang, K. Yu, J.A. Boscoboinik, Y. Liu, X. Liu, A.I. Frenkel, O.A. Abdelrahman, R. J. Gorte, S. Caratzoulas, D.G. Vlachos, Modulating the dynamics of Brønsted acid sites on PtWOₓ inverse catalyst, Nat. Catal. 5 (2022) 144–153, https://doi.org/10.1038/s41929-022-00745-y.

[9] Y. Wu, S. Sourav, A. Worrad, J. Zhou, S. Caratzoulas, G. Tsilomelekis, W. Zheng, D. G. Vlachos, Dynamic formation of Brønsted acid sites over supported WOₓ/Pt on SiO₂ inverse catalysts—spectroscopy, probe chemistry, and calculations, ACS Catal. 13 (2023) 7371–7382, https://doi.org/10.1021/acscatal.3c00279.

[10] Z. Lin, S. Deshpande, S.R. Denny, W.N. Porter, C. Wang, J. Marlowe, P. Christopher, W. Zheng, S. Caratzoulas, D.G. Vlachos, J.G. Chen, Mechanistic understanding of ring-opening of tetrahydrofurfuryl alcohol over WOₓ-modified Pt model surfaces and powder catalysts, ACS Catal. 13 (2023) 8014–8024, https://doi.org/10.1021/acscatal.3c01287.

[11] C. Wang, J.D. Lee, Y. Ji, T.M. Onn, J. Luo, C.B. Murray, R.J. Gorte, A study of tetrahydrofurfuryl alcohol to 1,5-pentanediol over Pt–WOₓ/C, Catal. Lett. 148 (2018) 1047–1054, https://doi.org/10.1007/s10562-018-2323-6.

[12] D.D. Falcone, J.H. Hack, A.Y. Klyushin, A. Knop-Gericke, R. Schlögl, R.J. Davis, Evidence for the bifunctional nature of Pt–Re catalysts for selective glycerol hydrogenolysis, ACS Catal. 5 (2015) 5679–5695, https://doi.org/10.1021/acscatal.5b01371.

[13] S. Koso, H. Watanabe, K. Okumura, Y. Nakagawa, K. Tomishige, Comparative study of Rh–MoOₓ and Rh–ReOₓ supported on SiO₂ for the hydrogenolysis of ethers and polyols, Appl. Catal. B: Environ. 111 (2012) 27–37, https://doi.org/10.1016/j.apcatb.2011.09.015.

[14] L. Liu, S. Kawakami, Y. Nakagawa, M. Tamura, K. Tomishige, Highly active iridium–rhenium catalyst condensed on silica support for hydrogenolysis of glycerol to 1,3-propanediol, Appl. Catal. B: Environ. 256 (2019) 117775, https://doi.org/10.1016/j.apcatb.2019.117775.

[15] Y. Amada, Y. Shinmi, S. Koso, T. Kubota, Y. Nakagawa, K. Tomishige, Reaction mechanism of the glycerol hydrogenolysis to 1,3-propanediol over Ir–ReOₓ/SiO₂ catalyst, Appl. Catal. B: Environ. 105 (2011) 117–127, https://doi.org/10.1016/j.apcatb.2011.04.001.

[16] Y. Nakagawa, Y. Shinmi, S. Koso, K. Tomishige, Direct hydrogenolysis of glycerol into 1,3-propanediol over rhenium-modified iridium catalyst, J. Catal. 272 (2010) 191–194, https://doi.org/10.1016/j.jcat.2010.04.009.

[17] Y. Nakagawa, M. Tamura, K. Tomishige, Catalytic reduction of biomass-derived furanic compounds with hydrogen, ACS Catal. 3 (2013) 2655–2668, https://doi.org/10.1021/cs400616p.

[18] K. Tomishige, Y. Nakagawa, M. Tamura, Selective hydrogenolysis and hydrogenation using metal catalysts directly modified with metal oxide species, Green. Chem. 19 (2017) 2876–2924, https://doi.org/10.1039/C7GC00620A.

[19] M. Chia, Y.J. Pagan-Torres, D. Hibbitts, Q. Tan, H.N. Pham, A.K. Datye, M. Neurock, R.J. Davis, J.A. Dumesic, Selective hydrogenolysis of polyols and cyclic ethers over bifunctional surface sites on rhodium-rhenium catalysts, J. Am. Chem. Soc. 133 (2011) 12675–12689, https://doi.org/10.1021/ja2038358.

[20] S. Koso, I. Furikado, A. Shimao, T. Miyazawa, K. Kunimori, K. Tomishige, Chemoselective hydrogenolysis of tetrahydrofurfuryl alcohol to 1,5-pentanediol, Chem. Commun. 15 (2009) 2035–2037, https://doi.org/10.1039/B822942B.

[21] Z. Lin, S. Liu, S.R. Denny, W.N. Porter, S. Caratzoulas, J.A. Boscoboinik, D. G. Vlachos, J.G. Chen, Experimental and theoretical insights into the active sites on WOₓ/Pt(111) surfaces for dehydrogenation and dehydration reactions, ACS Catal. 11 (2021) 8023–8032, https://doi.org/10.1021/acscatal.1c01061.

[22] W. Zhou, Y. Li, X. Wang, D. Yao, Y. Wang, S. Huang, W. Li, Y. Zhao, S. Wang, X. Ma, Insight into the nature of Brönsted acidity of Pt-(WOₓ)ₙ-H model catalysts in glycerol hydrogenolysis, J. Catal. 388 (2020) 154–163, https://doi.org/10.1016/j.jcat.2020.05.019.

[23] W. Zhou, J. Luo, Y. Wang, J. Liu, Y. Zhao, S. Wang, X. Ma, WOₓ domain size, acid properties and mechanistic aspects of glycerol hydrogenolysis over Pt/WOₓ/ZrO₂, Appl. Catal. B: Environ. 242 (2019) 410–421, https://doi.org/10.1016/j.apcatb.2018.10.006.

[24] J. Zhou, A. Worrad, Y. Wang, K. Yu, S. Deshpande, J.A. Boscoboinik, S. Caratzoulas, W. Zheng, D.G. Vlachos, The role of the metal core in the performance of WOₓ inverse catalysts, Chem. Catal. (2023) 100756, https://doi.org/10.1016/j.checat.2023.100756.

[25] J. Guan, G. Peng, Q. Cao, X. Mu, Role of MoO₃ on a Rhodium catalyst in the selective hydrogenolysis of biomass-derived tetrahydrofurfuryl alcohol into 1,5-pentanediol, J. Phys. Chem. C 118 (2014) 25555–25566, https://doi.org/10.1021/jp508313y.

[26] A.H. Larsen, J.J. Mortensen, J. Blomqvist, I.E. Castelli, R. Christensen, M. Dulak, J. Friis, M.N. Groves, B. Hammer, C. Hargus, E.D. Hermes, P.C. Jennings, P. B. Jensen, J. Kermode, J.R. Kitchin, E.L. Kolsbjerg, J. Kubal, K. Kaasbjerg, S. Lysgaard, J.B. Maronsson, T. Maxson, T. Olsen, L. Pastewka, A. Peterson, C. Rostgaard, J. Schiotz, O. Schutt, M. Strange, K.S. Thygesen, T. Vegge, L. Vilhelmsen, M. Walter, Z. Zeng, K.W. Jacobsen, The atomic simulation environment-a Python library for working with atoms, J. Phys. Condens. Matter 29 (2017) 273002, https://doi.org/10.1088/1361-648X/aa680e.

[27] M.J. Ungerer, D. Santo-Carballal, A. Cadi-Essadek, C.G. Van Sittert, N.H. De Leeuw, Interaction of H₂O with the platinum Pt (001), (011), and (111) surfaces: a density functional theory study with long-range dispersion corrections, J. Phys. Chem. C. 123 (2019) 27465–27476, https://doi.org/10.1021/acs.jpcc.9b06136.

[28] J. He, S.P. Burt, M.R. Ball, I. Hermans, J.A. Dumesic, G.W. Huber, Catalytic C-O bond hydrogenolysis of tetrahydrofuran-dimethanol over metal supported WOₓ/TiO₂ catalysts, Appl. Catal. B: Environ. 258 (2019) 117945, https://doi.org/10.1016/j.apcatb.2019.117945.

[29] R. Huang, O. Kwon, C. Lin, R.J. Gorte, The effects of SMSI on m-Cresol hydrodeoxygenation over Pt/Nb₂O₅ and Pt/TiO₂, J. Catal. 398 (2021) 102–108, https://doi.org/10.1016/j.jcat.2021.04.012.

[30] D.A. Bulushev, M. Zacharska, A.S. Lisitsyn, O.Y. Podyacheva, F.S. Hage, Q. M. Ramasse, U. Bangert, L.G. Bulusheva, Single atoms of Pt-group metals stabilized by N-doped carbon nanofibers for efficient hydrogen production from formic acid, ACS Catal. 6 (2016) 3442–3451, https://doi.org/10.1021/acscatal.6b00476.

[31] M. Liu, W. Tang, Z. Xie, H. Yu, H. Yin, Y. Xu, S. Zhao, S. Zhou, Design of highly efficient Pt-SnO₂ hydrogenation nanocatalysts using Pt@Sn Core–Shell nanoparticles, ACS Catal. 7 (2017) 1583–1591, https://doi.org/10.1021/acscatal.6b03109.

[32] W.D. Michalak, J.M. Krier, S. Alayoglu, J.-Y. Shin, K. An, K. Komvopoulos, Z. Liu, G.A. Somorjai, CO oxidation on PtSn nanoparticle catalysts occurs at the interface of Pt and Sn oxide domains formed under reaction conditions, J. Catal. 312 (2014) 17–25, https://doi.org/10.1016/j.jcat.2014.01.005.

[33] J. Zhou, Y. Zhao, J. Zhang, Y. Wang, O.Y. Gutierrez, S. Wang, Z. Li, P. Jin, S. Wang, X. Ma, J.A. Lercher, A nitrogen-doped PtSn nanocatalyst supported on hollow silica spheres for acetic acid hydrogenation, Chem. Commun. 54 (2018) 8818–8821, https://doi.org/10.1039/C8CC03649G.

[34] A. Rajan, J.J. Varghese, Towards selective glycerol hydrodeoxygenation to 1,3-propanediol with effective Pt-WOₓ catalyst design: Insights from first principles, J. Catal. 423 (2023) 94–104, https://doi.org/10.1016/j.jcat.2023.04.019.

[35] T. Buntara, I. Melián-Cabrera, Q. Tan, J.L.G. Fierro, M. Neurock, J.G. de Vries, H. J. Heeres, Catalyst studies on the ring opening of tetrahydrofuran–dimethanol to 1,2,6-hexanetriol, Catal. Today 210 (2013) 106–116, https://doi.org/10.1016/j.cattod.2013.04.012.

[36] S. Koso, Y. Nakagawa, K. Tomishige, Mechanism of the hydrogenolysis of ethers over silica-supported rhodium catalyst modified with rhenium oxide, J. Catal. 280 (2011) 221–229, https://doi.org/10.1016/j.jcat.2011.03.018.

[37] M. Chia, B.J. O'Neill, R. Alamillo, P.J. Dietrich, F.H. Ribeiro, J.T. Miller, J. A. Dumesic, bimetallic RhRe/C catalysts for the production of biomass-derived chemicals, J. Catal. 308 (2013) 226–236, https://doi.org/10.1016/j.jcat.2013.08.008.